ACS APPLIED MATERIALS & INTERFACES

www.acsami.org Research Article

Reversal of the Direction of Rectification Induced by Fermi Level Pinning at Molecule−Electrode Interfaces in Redox-Active Tunneling Junctions

Yingmei Han,[#] Maria Serena Maglione,[#] Valentin Diez Cabanes,[#] Javier Casado-Montenegro, Xiaojiang Yu, Senthil Kumar Karuppannan, Ziyu Zhang, Núria Crivillers, Marta Mas-Torrent, Concepció Rovira, Jérôme Cornil,* Jaume Veciana,* and Christian A. Nijhuis*

Cite This: https://dx.doi.org/10.1021/acsami.0c15435 Read Online

ACCESS | Metrics & More | Article Recommendations | Supporting Information

ABSTRACT: Control over the energy level alignment in molecular junctions is notoriously difficult, making it challenging to control basic electronic functions such as the direction of rectification. Therefore, alternative approaches to control electronic functions in molecular junctions are needed. This paper describes switching of the direction of rectification by changing the bottom electrode material M = Ag, Au, or Pt in M−S$(CH_2)_{11}$S−BTTF//EGaIn junctions based on self-assembled monolayers incorporating benzotetrathiafulvalene (BTTF) with EGaIn (eutectic alloy of Ga and In) as the top electrode. The stability of the junctions is determined by the choice of the bottom electrode, which, in turn, determines the maximum applied bias window, and the mechanism of rectification is dominated by the energy levels centered on the BTTF units. The energy level alignments of the three junctions are similar because of Fermi level pinning induced by charge transfer at the metal−thiolate interface and by a varying degree of additional charge transfer between BTTF and the metal. Density functional theory calculations show that the amount of electron transfer from M to the lowest unoccupied molecular orbital (LUMO) of BTTF follows the order Ag > Au > Pt. Junctions with Ag electrodes are the least stable and can only withstand an applied bias of ±1.0 V. As a result, no molecular orbitals can fall in the applied bias window, and the junctions do not rectify. The junction stability increases for M = Au, and the highest occupied molecular orbital (HOMO) dominates charge transport at a positive bias resulting in a positive rectification ratio of 83 at ±1.5 V. The junctions are very stable for M = Pt, but now the LUMO dominates charge transport at a negative bias resulting in a negative rectification ratio of 912 at ±2.5 V. Thus, the limitations of Fermi level pinning can be bypassed by a judicious choice of the bottom electrode material, making it possible to access selectively HOMO- or LUMO-based charge transport and, as shown here, associated reversal of rectification.

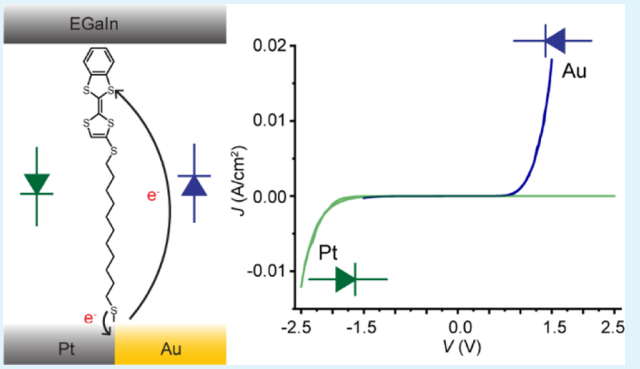

KEYWORDS: *molecular diodes, molecular electronics, charge transfer, energy level alignment, Fermi-level pinning*

INTRODUCTION

The mechanisms of charge transport and transfer are fundamental to understanding various areas of research ranging from catalysis[1] and biology[2] to energy management.[3] Molecular tunnel junctions make it possible to uncover and study new phenomena, such as light-matter interactions in tunnel junctions,[4,5] conductance switching,[6,7] molecular sensing,[8] or new mechanisms of charge transport (such as long-range tunneling,[9,10] charge transport in the inverted Marcus region,[11,12] or nuclear tunneling[13,14]), at the molecular length scales. It is still a challenge to control the energy level alignment within molecular junctions as it depends on several intertwined factors related to molecule−electrode interactions involving push back effects,[15,16] Fermi level (E_f) pinning,[16,17] (partial) charge transfer between the molecule and the surface,[15,18] formation of surface dipoles and the role of molecular dipoles,[19,20] or collective electrostatic effects,[21,22] complicating the rational design of molecular junctions. For these reasons, it is challenging to control basic electronic functions of molecular junctions, such as the direction of rectification.

Received: August 27, 2020
Accepted: October 30, 2020

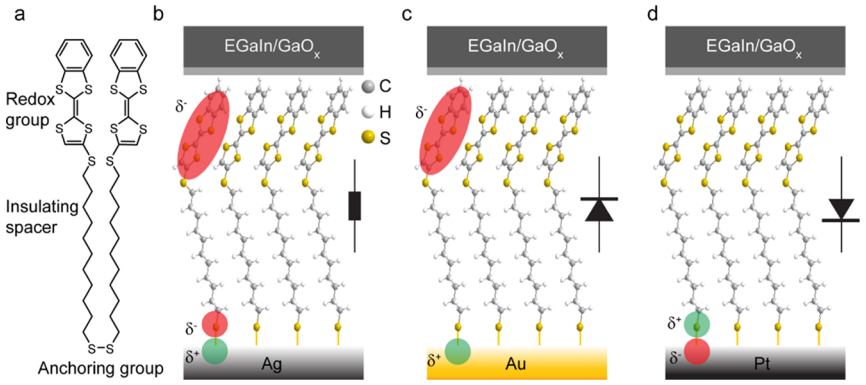

Figure 1. (a) Molecular structure of $(S(CH_2)_{11}S{-}BTTF)_2$. (b–d) Schematic illustrations of $M{-}S(CH_2)_{11}S{-}BTTF//GaO_x/EGaIn$ junctions with M = Ag, Au, and Pt. Red and green ovals indicate negative and positive charges after partial charge transfer as a result of energy level alignment, respectively. The circuit symbols indicate the direction of rectification or when the junction does not rectify (and behaves as a resistor). δ^+ and δ^- indicate partial charge transfer between the S and BTTF units and the bottom electrode surface as determined from DFT calculations (see Figure 4). There is no direct charge transfer between the Pt electrode and the BTTF unit.

Molecular rectification has been one of the hallmarks in molecular electronics since the landmark report by Aviram and Ratner, which outlines the theoretical basis of a molecular diode.[23] Although well-performing molecular diodes based on, for example, donor–acceptor (D–A) compounds,[11,24] large molecular dipoles,[25,26] different interface dipoles,[27] or redox-units,[28,29] have been reported, control over the direction of rectification is limited. The direction of rectification is defined as the bias at which the molecular diodes allow the current to pass through the junctions given by

$$R^+ = J(+V)/J(-V) \tag{1a}$$

$$R^- = J(-V)/J(+V) \tag{1b}$$

where J is the current density that flows across the junctions as a function of the applied voltage V. Here, R^+ is the rectification ratio for a junction that allows the current to pass through at positive V but blocks the current at negative V, and R^- defines the same but for a junction with reversed rectification. So far, only a few examples have been reported where reversal of rectification has been demonstrated. In large area junctions, the redox group is typically located at the top of the monolayer and is therefore in close proximity to the top electrode. Reversal of rectification has been achieved in such systems by moving the redox unit to the bottom of the monolayer.[30,31] Similarly, reversal of rectification has been achieved by moving a dipole from the top to the bottom of the monolayer.[25] In junctions with D–A compounds, changing the orientation of the D–A unit with respect to the electrodes also results in reversal of rectification.[24,32] All these strategies require modification of the chemical structure of the molecules *via* elaborate chemical synthesis. In contrast, here we report reversal of rectification by simply changing the bottom electrode material.

The energy level alignment at metal–molecule interfaces involves the formation of interface dipoles (Δ) due to push back effects (molecular adsorption on the metal, which "pushes" back the electron into the metal), which systematically lowers the work function of the metal electrode (Φ) (although this effect may be compensated when, for instance, back-bonding from the metal dominates[17,18]). Often, charge transfer between the molecule and the metal surface has also to be considered since it affects the interface dipole and may increase or lower Φ.[16,33,34] For instance, in alkanethiolate self-assembled monolayers (SAMs) on coinage metals, charge transfer occurs between the metal and the thiolate and results in a well-known Fermi level pinning due to the strong interfacial electronic coupling, implying that the work function of the metal after molecular adsorption is independent of the work function of the native metal. In principle, when redox-active units are present, charge transfer between the metal surface and the highest occupied molecular orbital (HOMO) or the lowest unoccupied molecular orbital (LUMO) centered on the redox units may also occur.

Because of the Fermi level pinning effects, one would expect that the mechanism of charge transport is independent of M. Whitesides and co-workers showed that the mechanism of electrical failure of molecular junctions is independent of the molecular structure;[35] we have recently shown that the breakdown mechanism is dominated by direct transfer of momentum of the conduction electrons to the atoms in the electrodes *via* the wind force resulting in metal filament formation.[36] These studies indicated that the stability of the junctions can be improved by judiciously choosing the bottom electrode materials. Therefore, by changing the electrode material of the junctions, it should be possible to increase the bias window and access different charge-transport regimes and behaviors. This paper describes reversal of the direction of rectification of molecular diodes of the form $M{-}S(CH_2)_{11}S{-}BTTF//GaO_x/EGaIn$ (BTTF = benzotetrathiafulvalene, EGaIn = eutectic alloy of Ga and In, and M = Ag, Au, or Pt) depending on the choice of the bottom electrode material M. Figure 1 shows schematic illustrations of the junctions and indicates the partial charge transfer from the metal to the BTTF units that is made possible by a super exchange mechanism;[37,38] this partial charge transfer is large for M = Ag, moderate for M = Au, and negligible for M = Pt, resulting in a similar energy level alignment for the three bottom electrodes. Junctions with Ag electrodes can only withstand a narrow bias window of ±1.0 V and do not rectify. Junctions with M = Au are more stable with a rectification ratio R^+ = 83 at ±1.5 V involving the HOMO. In contrast, junctions with M = Pt are very stable, and the current flows across the junction at negative bias with R^- = 912 at ± 2.5 V by involving the LUMO. These results show that it is possible to control the direction of rectification, despite Fermi level pinning, by changing the bottom electrode material.

https://dx.doi.org/10.1021/acsami.0c15435
ACS Appl. Mater. Interfaces XXXX, XXX, XXX–XXX

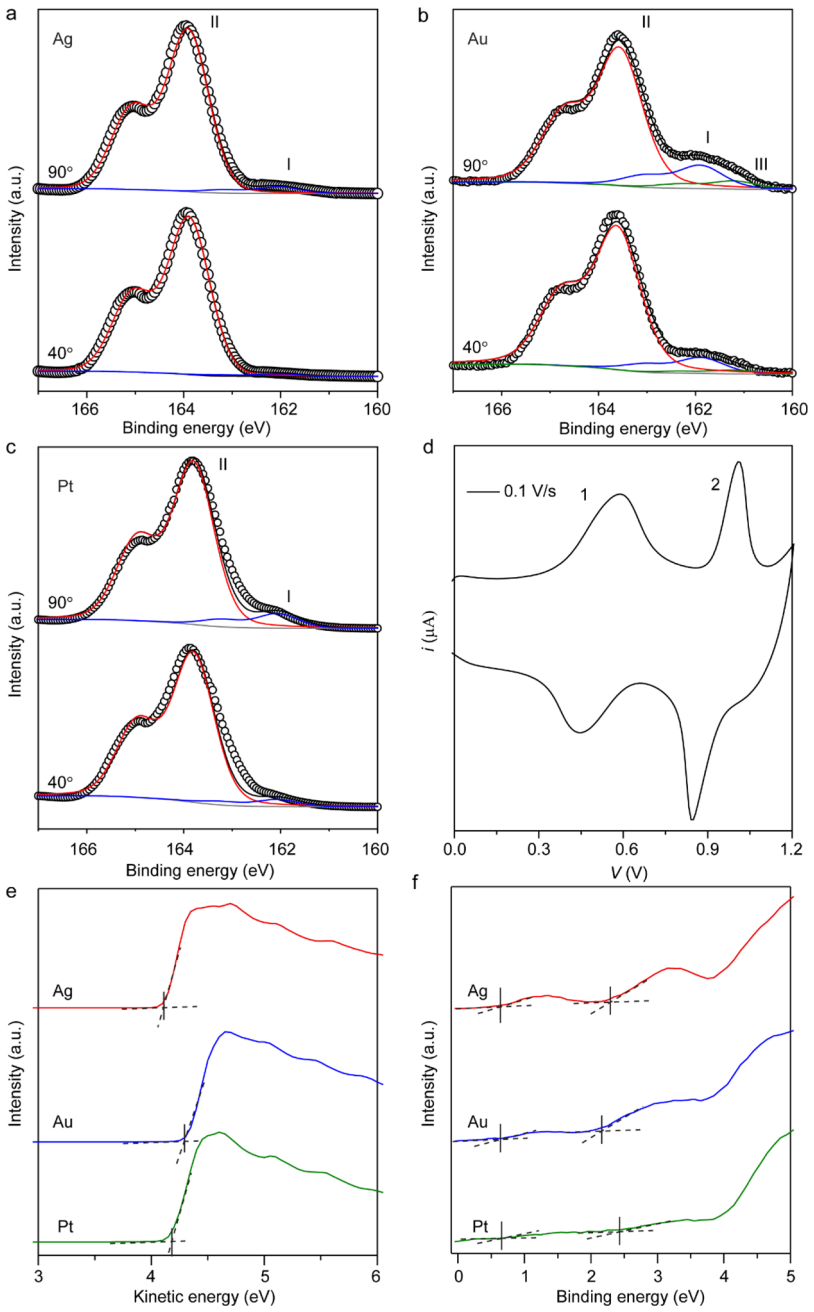

Figure 2. S 2*p* spectra of $S(CH_2)_{11}S$–BTTF SAMs on Ag (a), Au (b), and Pt (c) at take-off angles of 90 and 40°. (d) CV of $S(CH_2)_{11}S$–BTTF SAMs on Au at 0.1 V/s. (e) SECO spectra of $S(CH_2)_{11}S$–BTTF SAMs on Ag, Au, and Pt. (f) Valence band spectra of BTTF SAMs on Ag, Au, and Pt (see Figure S11 for full valence band spectra). The HOMO and HOMO − 1 onsets are marked with black lines.

RESULTS AND DISCUSSION

Structural Characterization of BTTF SAMs. The synthesis and characterization of the $(S(CH_2)_{11}S–BTTF)_2$ SAM precursor is described in detail in Section S1. The SAMs were formed on template-stripped Ag, Au, and Pt following a well-established procedure (Section S2) and characterized in detail (Section S3). Despite the fact that the three types of surfaces have similar surface roughness, the surface topography of the three metal surfaces is different, with the Ag surface having large grains and grain boundaries, while the grain sizes and grain boundaries of Au and Pt are very small. We have reported before[39] that the performance of molecular junctions with large grains and grain boundaries is similar to that of junctions with small grains and grain boundaries because the fraction of exposed grain boundaries in the former case is small.[29,40] Figure 2 shows the angle-resolved X-ray photoelectron spectroscopy (AR XPS) results for the S 2*p* signals for the SAMs on the three different bottom electrodes recorded at normal (90°) and grazing (40°) take-off angles (see Section S3 for the C 1*s*, Ag 3*d*, Au 4*f*, and Pt 4*f* spectra). The spectra are dominated by two doublets each consisting of the S $2p_{1/2}$ and S $2p_{3/2}$ signals with the characteristic intensity ratio of 1:2. We assigned peak I with a binding energy of ∼162.0 eV (blue line) to the metal–thiolate bond and peak II with a binding energy of ∼163.9 eV (red line) to the five sulfur atoms at the top of $S(CH_2)_{11}S$–BTTF SAMs and the physisorbed sulfur species, following previous peak assignments.[41] For $S(CH_2)_{11}S$–BTTF SAMs on Au, a small peak III (green line) at 161.2 eV is

https://dx.doi.org/10.1021/acsami.0c15435
ACS Appl. Mater. Interfaces XXXX, XXX, XXX−XXX

Table 1. Summary of Electronic Properties of $S(CH_2)_{11}S$−BTTF SAMs[a]

	UPS and NEXAFS							DFT						
metal	Φ_{SAM} [eV]	δE_H [eV]	E_H [eV]	δE_{H-1} [eV]	E_{H-1} [eV]	δE_L [eV]	E_L [eV]	Φ_{SAM} [eV]	δE_H [eV]	E_H [eV]	δE_{H-1} [eV]	E_{H-1} [eV]	δE_L [eV]	E_L [eV]
Ag	4.08	0.59	−4.67	2.31	−6.39	1.84	−2.24	4.01	0.12	−4.12	1.47	−5.48	2.16	−1.85
Au	4.31	0.60	−4.91	2.15	−6.46	2.25	−2.06	4.03	0.10	−4.12	1.45	−5.48	2.2	−1.83
Pt	4.16	0.62	−4.78	2.42	−6.58	1.83	−2.33	3.99	0.11	−4.10	1.49	−5.48	2.25	−1.74

[a]More technical details about the DFT (functional, *k*-point sampling, pseudopotentials, cutoffs) and unit cell (lattice parameters, surface coverages) parameters used in our calculations are given in Section S5 of the Supporting Information.

visible, which is attributed to the Au−S bond associated with a disordered chemisorbed phase.[42] The XPS spectra recorded with 40° take-off angle show that the intensity of peak I decreases with respect to peak II (Figure 2), confirming that peak I originates from sulfur species close to the metal surface (Au−S) and that peak II originates from sulfur species located at the top of the SAMs.

From the AR XPS data, we determined the values of the SAM thickness d_{SAM} (Section S3) along the surface normal on Ag, Au, and Pt. The values of d_{SAM} are similar with experimental error (21 ± 3 Å for Ag and Pt; 26.1 ± 3 Å for Au) and comparable to the molecular length (21.6 Å) calculated using the CPK model and a tilt angle (relative to the surface normal) of 57° determined by near edge X-ray absorption fine structure (NEXAFS). We note that the somewhat larger value of d_{SAM} for Au originates from the disorder observed in the aforementioned XPS data. We found that the surface coverage (Γ_{BTTF}) of $S(CH_2)_{11}S$−BTTF SAMs relative to the values determined from cyclic voltammogram (CV) (Section S3) is similar for all three metal surfaces (on average $\Gamma_{BTTF} = 1.88 \times 10^{-10}$ mol/cm^2; Table S1). The similar tilt angle and surface coverage suggest that the SAM packing is driven by $\pi-\pi$ interactions between the BTTF units rather than differences in the M−S bond geometries, alkyl−alkyl chain interactions, or gauche effects.[43−45]

Figure 2d shows the CV of the $S(CH_2)_{11}S$−BTTF SAMs on Au measured at a scan rate of 0.1 V/s. The CV exhibits two pairs of redox peaks with peak anodic/cathodic redox potentials (E_{pa}/E_{pc}) of +0.59/+0.44 and +1.01/+0.84 V; these values are similar to those values determined with $(S(CH_2)_{11}S-BTTF)_2$ in solution (Section S3). We assign peaks 1 and 2 to the oxidation of the BTTF unit to the radical cation and the dication, respectively, similar to SAMs with tetrathiafulvalene (TTF) termini.[46] The full width at half-maximum (fwhm) of the second oxidation peak of the $S(CH_2)_{11}S$−BTTF SAMs on Au (88 mV) is smaller than that of the first oxidation peak (167 mV). A similar behavior has also been observed in the CVs of other TTF SAMs on Au.[46,47] For a reversible one-electron redox process, the fwhm is 90.6 mV (at 25 °C),[48] but here the broadening indicates strong repulsive electrostatic interactions between neighboring BTTF units, similar to previously reported SAMs with TTF termini.[49] The system shows quasi-reversible behavior as the peak oxidation and reduction potentials of both peaks increase with increasing scan rates, which indicates sluggish heterogeneous electron transfer rates likely caused by the presence of the long alkyl chain (Figure S13). Based on all these observations, we conclude that the SAMs are densely packed and that the standing up phase dominates the SAM structure. Some of us have reported before that SAMs derived from disulfides ($(S-(CH_2)_{11}Fc)_2$) have a lower surface coverage than those SAMs derived from the corresponding thiols ($HS-(CH_2)_{11}Fc$) with ferrocene (Fc) head groups.[42] In contrast, the BTTF SAMs reported here readily form dense monolayers likely driven by favorable $\pi-\pi$ interactions between neighboring BTTF units (which explains the similar tilt angles of the BTTF units of 57° measured with NEXAFS).

Electronic Structure of the SAMs. Figure 2e,f shows the secondary electron cutoff spectra (SECO) and the valence band, respectively (Section S3). For $S(CH_2)_{11}S$−BTTF SAMs on Ag, two features just below the Fermi edge at a binding energy of 0.59 and 2.3 eV are visible. Based on previous peak assignments of ultraviolet photoelectron spectra (UPS) of TTF,[50] we assign these two features to the HOMO and HOMO − 1 from which we determined the energies of these levels with respect to vacuum, E_H and E_{H-1}, respectively (Table 1). The intensities of the HOMO and HOMO − 1 features for the SAMs on Au are smaller than those on Ag and barely visible for SAMs on Pt. As discussed in detail below, density functional theory (DFT) calculations indicate that the different degrees of hybridization between the molecular HOMO and HOMO − 1 levels and the continuum of states of the metal electrode are responsible for this behavior (Section S5). We note that a similar decrease in the intensity of the HOMO and HOMO − 1 features has been observed due to charge transfer between TTF and tetracyanoquinodimethane (TCNQ) in TCNQ−TTF charge-transfer crystals.[50] We also determined the energy offsets between HOMO and HOMO − 1 and the Fermi level of the electrode, δE_H and δE_{H-1}, which are similar for SAMs on Ag, Au, and Pt (Table 1). These energy offsets are comparable to what has been reported for TTF-based SAMs on Au.[41,51] From the SECO spectra, we determined the work function Φ_{SAM} of the SAM-modified bottom electrodes (Section S3). Table 1 shows that Φ_{SAM} for Ag and Pt surfaces are close to 4.1 eV, while for the Au surface, Φ_{SAM} is 0.2 eV larger, which we attribute to the disorder of these SAMs, as discussed earlier. Despite the large differences between the values of Φ_M of the bare metal ranging from 4.2 eV for Ag to 5.75 eV for Pt (Table 2), the values of Φ_{SAM} are similar, which can be explained by Fermi level pinning, as discussed in more detail below.

The energy of the LUMO (E_L) was extracted for all three SAMs from the first resonant peak in NEXAFS spectra by following previously reported procedures (Section S3) and is

Table 2. Calculated Electronic Properties for the $S(CH_2)_{11}S$−BTTF SAMs Adsorbed on Ag, Au, and Pt Metal Surfaces

M	E_{ads} (eV)	Φ_M (eV)	Φ_{SAM} (eV)	Δ_Φ (eV)	ΔV_{SAM} (eV)	BD (eV)
Ag	−2.32	4.2	4.01	−0.19	−1.65	1.46
Au	−2.22	5.2	4.03	−1.18	−1.64	0.47
Pt	−3.3	5.75	3.99	−1.76	−1.68	−0.08

https://dx.doi.org/10.1021/acsami.0c15435
ACS Appl. Mater. Interfaces XXXX, XXX, XXX−XXX

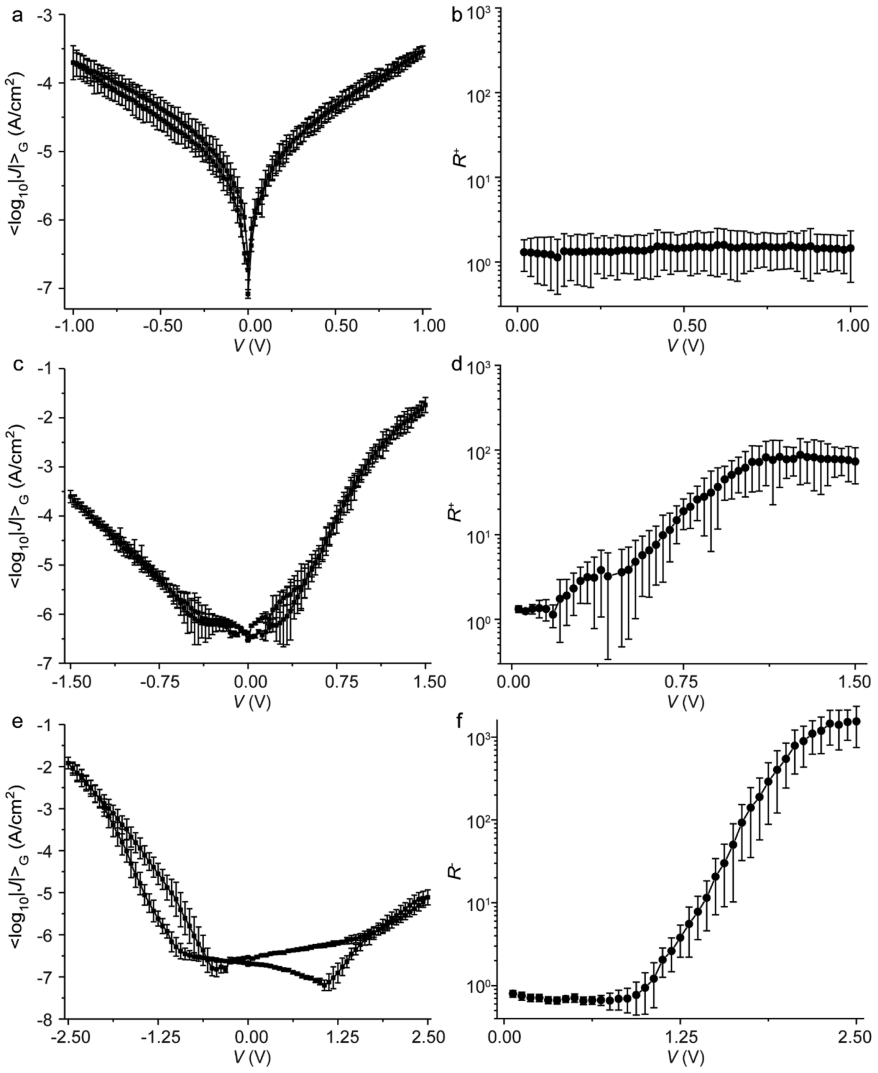

Figure 3. Plots of $\langle \log_{10}|J| \rangle_G$ vs V and $R(V)$ plots obtained from M−S$(CH_2)_{11}$S−BTTF//GaO_x/EGaIn junctions where M = Ag (a,b), Au (c,d), and Pt (e,f). The error bars represent 95% confidence levels (Section S4). These data are collected based on 26 working junctions (out of 29) for M = Ag, 26 working junctions (out of 31) for M = Au, and 31 working junctions (out of 39) for M = Pt.

listed in Table 1. The experimentally determined HOMO−LUMO gap from UPS and NEXAFS varies from 2.4 to 2.8 eV (Table 1) and is comparable to the measured optical HOMO−LUMO gap of 2.99 eV (Section S3) with UV−vis spectroscopy. We note that the HOMO−LUMO gap measurements are rough estimates because of core-hole (in NEXAFS) and exciton (in UV−vis) interactions, but qualitatively the different experimental values agree.

Electrical Characterization of the Junctions. The junctions were fabricated by contacting the SAMs with cone-shaped EGaIn tips (Figure 1) following a previously reported procedure[29] (Section S4). The current density (J) versus voltage (V) curves were recorded in the bias window of ±1.0 V for junctions on Ag, ±1.5 V for junctions on Au, and ±2.5 V for junctions on Pt; these bias voltage ranges are below the breakdown voltages of EGaIn junctions with these bottom electrodes.[36] Table S3 summarizes the yields of working junctions, the number of junctions, and traces that were recorded and statistically analyzed following previously reported procedures to obtain the Gaussian log−average $J(V)$ curves ($\langle \log_{10}|J| \rangle_G$ (V)) along with the Gaussian log−standard deviations and 95% confidence levels shown in Figure 3.[6,29,52] Similarly, we also constructed the histograms of $\log_{10}|R|$ at ±1.0 V for M = Ag, ±1.5 V for M = Au, and ±2.5 V for M = Pt to determine $\langle \log_{10}|R| \rangle_G$ and $\sigma_{\log}$ (Section S4).

The most striking result is that for junctions with M = Ag, no rectification is observed, while for junctions with M = Au, the value of R^+ is 83 ($\sigma_{\log} = 0.29$), and for M = Pt, the value of $R^- = 9.1 \times 10^2$ ($\sigma_{\log} = 0.76$). In other words, the direction of rectification is reversed for junctions with M = Au or Pt, implying that junctions with M = Au allow the current to flow across the junction at a positive bias, while the opposite is true for junctions with M = Pt. The values of J for the junctions with the Ag electrode are low, which indicates that within the bias window of ±1.0 V, no molecular frontier orbitals enter the conduction window. In contrast, for junctions with Au and Pt electrodes, a large increase in the J value is observed around 0.50 and 0.90 V, respectively, which indicates that at these voltages, a molecular frontier orbital enters the conduction window (see below). This increase in the J value in only one bias polarity is reflected in the corresponding $R(V)$ plots (Figure 3).

Computational Modeling of SAMs. We performed DFT calculations to shed light on the electronic properties of the

https://dx.doi.org/10.1021/acsami.0c15435
ACS Appl. Mater. Interfaces XXXX, XXX, XXX−XXX

$S(CH_2)_{11}S$−BTTF based SAMs adsorbed on Ag, Au, and Pt surfaces (Section S5). The optimized structures display very similar geometric parameters (Figures S16 and 17 and Tables S4 and S5) of the $S(CH_2)_{11}S$−BTTF molecules within the SAM, as expected by the fact that the three metals are characterized by very similar lattice parameters. This is in line with the experimental observations pointing to similar degrees of coverage, SAM thickness, and tilt angles for the three studied SAMs. The only appreciable difference is the metal−sulfur bond distance, which in the case of Pt is about 0.2 Å shorter with respect to Ag and Au surfaces as reported by others.[53] Because of the stronger Pt−S bonds, Pt−$S(CH_2)_{11}S$−BTTF-based SAMs are more stable (1.0 eV difference in the adsorption energy E_{ads}) compared with the other metal surfaces (Table S5).

Next, we computed the values of Φ_{SAM} (i.e., with $S(CH_2)_{11}S$−BTTF layers adsorbed on the three different surfaces). All Φ_{SAM} values are similar and close to 4.0 eV because of the Fermi level pinning, which is consistent with the Φ_{SAM} values determined with UPS (~4.2 eV) despite the large differences in the work functions of the native metals (Φ_M in Table 2).

To elucidate the nature of the work function shifts induced by the SAMs ($\Delta\Phi$), we casted down the total shift in two contributions originating from eq 2: (i) the permanent dipole (ΔV_{SAM}) of the molecular backbone (i.e., dipole mostly oriented along the BTTF unit) and (ii) the bond dipole (BD) contribution which is the potential shift arising from the charge reorganization upon adsorption.

$$\Delta\Phi = \Delta V_{SAM} + BD \tag{2}$$

The values of ΔV_{SAM} are identical (−1.65 eV) for the three studied surfaces because of the similar geometric pattern of the $S(CH_2)_{11}S$−BTTF layers. For that reason, the origin of the pinning effect mentioned above is exclusively due to interfacial charge transfer upon adsorption. Variations in M−S dipole balancing the work function for different metals after SAM deposition has also been observed for oligophenylene thiol SAMs both at experimental[54] and theoretical[55] levels. Furthermore, this effect was also found in perylene diimide SAMs with isocyanide anchoring groups.[56]

We have analyzed the differences in charge density redistribution at the metal−molecule interfaces upon deposition of the SAM by following the so-called radical scenario (eq 3). In this formalism, the reorganization of the electron density at the interface ($\Delta\rho$ in $e^-/Å$) can be estimated as the difference between the electron density of the full system (ρ_{M-SAM}) and their individual components: the $S(CH_2)_{11}S$−BTTF layer (ρ_{SAM}) and the metal surface (ρ_M).

$$\Delta\rho = \rho_{M-SAM} - (\rho_M + \rho_{SAM}) \tag{3}$$

By cumulative integration of the electron density redistribution at the interface, we can estimate the charge-transfer profile at the interface (ΔQ in e^-). Finally, the progressive buildup of the BD contribution (BD in eV) along the normal direction with respect to the metal surface was obtained by applying the Poisson equation (eq 4), where ε_0 is the dielectric constant of vacuum.

$$\nabla^2 BD(z) = -\frac{\Delta\rho(z)}{\varepsilon_0} \tag{4}$$

Figure 4 shows the different profiles of the charge transfer at the interface depending on the metal surface. Interestingly,

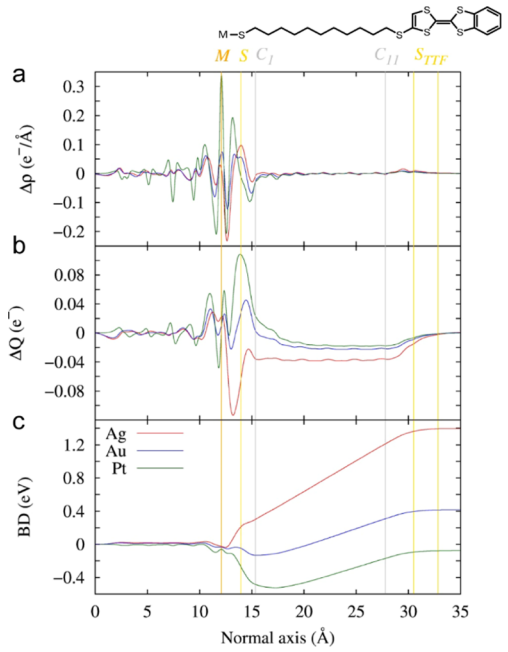

Figure 4. Plane-averaged charge density difference (a), cumulated charge transfer (b), and BD (c) profile at the interface along the normal axis to Ag (red), Au (blue), and Pt (green) metal surfaces. The vertical lines represent the atomic positions of the first metallic layer (orange), anchoring group S (yellow), the first C bonded to the S (C_1), and the C connected to the BTTF unit (C_{11}; gray).

both the magnitude and direction of the charge transfer change as a function of the nature of the metal surface: Ag and Au lose electron density, while Pt gains electron density. To obtain a quantitative estimation and a spatial representation of the charge-transfer mechanism, we performed a Hirshfeld versus Voronoi charge population analysis[57] (Tables S6 and S7). The magnitude of the charge transfer is −0.14, −0.02, and 0.18 e^- for M = Ag, Au, and Pt, respectively. These values are consistent with reported charge transfers found in other thiolate-based SAMs.[58,59] Despite the fact that M = Pt presents higher values for the charge transfer, the magnitude of the BD associated with this transfer is very low. Actually, the charge transfer for this surface is localized at the Pt−S interface, while in the case of Ag and Au, a charge transfer between the BTTF unit and the metal surface is also found in addition to that associated with the M−S bond (Figure S18).

Figure 5 shows the calculated energy level alignment of the M−$S(CH_2)_{11}S$−BTTF SAMs on Ag, Au, and Pt. The combined M−S dipole and the partial charge transfer from the electrodes to BTTF units shift the E_{HOMO} centered at the BTTF unit toward E_f, while E_{LUMO} is shifted away from E_f by an equal amount. The partial charge transfer to the BTTF unit is larger for M = Ag with respect to M = Au and M = Pt. Therefore, the shift in the potential associated with the interfacial charge transfer (BD) is 1.46, 0.47, and −0.08 eV for M = Ag, Au, and Pt respectively, which coincides with the above-mentioned shift experimented by the energetic levels of the molecules. Consequently, the energy level alignment of the three interfaces is similar despite the large difference in the work function of the native metals, in good agreement with experiments (Table 1). We note that the mechanism of

https://dx.doi.org/10.1021/acsami.0c15435
ACS Appl. Mater. Interfaces XXXX, XXX, XXX−XXX

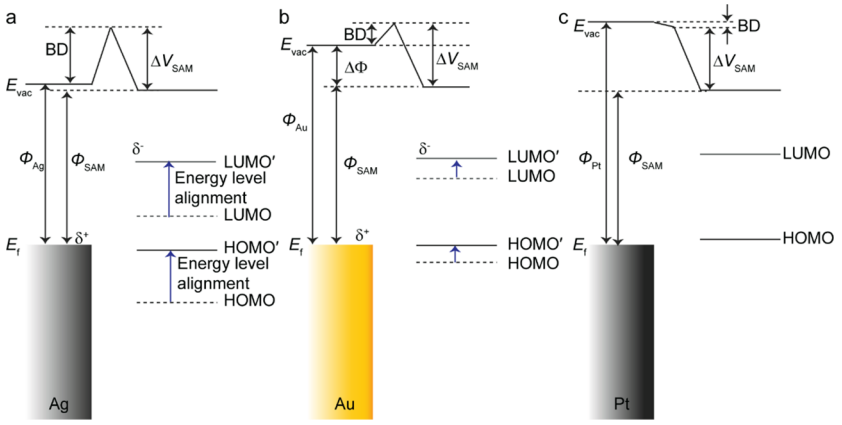

Figure 5. Computed energy level diagrams with E_{vac} = energy of vacuum, E_f = Fermi-level energy, and Φ_M = work function of metal [M = Ag (a), Au (b), and Pt (c)]. Φ_{SAM} = work function of the metal surface after SAM formation. HOMO and HOMO′ are the highest occupied molecular orbitals before (black dashed lines) and after (black solid line) charge transfer with the Ag, Au, and Pt bottom electrodes. LUMO (gray dashed lines) and LUMO' (gray solid line) are the corresponding lowest unoccupied molecular orbital levels.

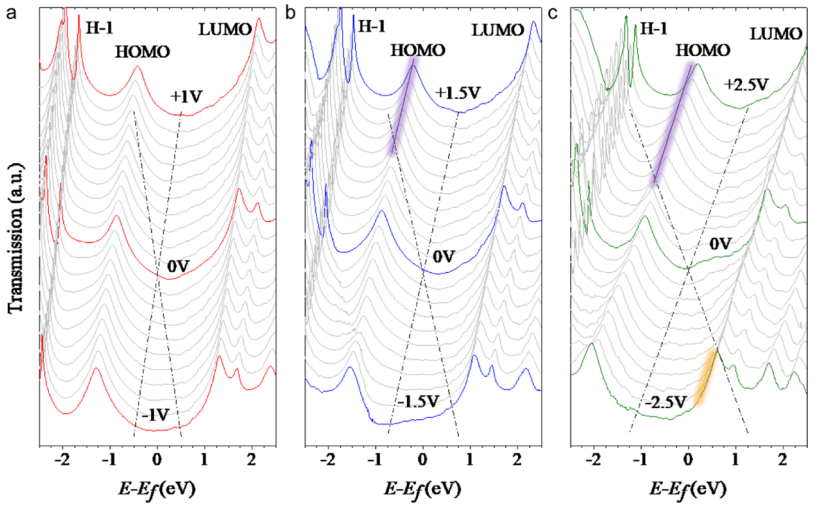

Figure 6. Transmission spectra across the M−S$(CH_2)_{11}$S−BTTF//Ag junctions as a function of the voltage difference applied to the electrodes for M = Ag (a), Au (b), and Pt (c). The cones delimited by the dashed lines depict the voltage windows applied to each junction: ±1 V for M = Ag, ± 1.5 V for M = Au, and ±2.5 V for M = Pt. The purple and orange shades indicate when the HOMO or LUMO falls in the bias window, respectively. Note that the molecular orbital energies are not necessarily coinciding with the energies of the transmission peaks. In the present case, no big differences are expected between these energies in view of the weak coupling between the BTTF moiety and both electrodes.

interfacial charge transfer between M and BTTF most likely proceeds via a super exchange mechanism well-known for donor−bridge−acceptor compounds;[37,38] here, the metal fulfils the role of the donor and BTTF that of the acceptor. This charge transfer does not reflect a formal reduction of the BTTF unit but actually corresponds to a fractional charge transfer.

In addition, the aforementioned pinning effect is at the origin of the similar energetic alignment with respect to the metal E_f in the three studied SAMs (Figure 5), as found by UPS measurements for Ag and Au metal surfaces. Nevertheless, the HOMO signals are barely visible in the UPS spectrum of Pt. The total density of states of the different SAMs shows that the states of Pt are very intense in the vicinity of E_f (Figures S19 and 20). Consequently, the hybridization of the S$(CH_2)_{11}$S−BTTF frontier occupied levels with the Pt surface is higher than for the other electrodes (Figure S21). This finding agrees with the higher amplitude of the oscillations in the evolution of $\Delta\rho$ with the normal distance with respect to that across the Ag and Au metal surfaces (Figure 4a) and with the shorter M−S bond distances. In summary, stronger coupling implies larger broadening of the molecular levels and hence a lower resolution in the UPS spectra.

Computational Modeling of the Molecular Junctions. To model the junction characteristics, we placed a Ag top electrode on top of the M−S$(CH_2)_{11}$S−BTTF SAMs with M = Ag, Au, and Pt (Figures S22 and S27) (Section S5) because Ag has a work function[60] (Φ_{Ag} = 4.25 eV) similar to that of the GaO_x/EGaIn top electrode[61] (Φ_{EGaIn} = 4.1−4.2 eV). We also verified that replacing Ga−In with Ag top contacts has only a marginal effect on the transmission properties of the junctions (Figures S27 and S28). However, our results are sensitive to the choice of van der Waals distance between the SAM and the top contact (Figures S31−S33). In our calculations, we used an optimized distance of 2.5 Å as discussed in Section S6 and computed the transmission spectra at the equilibrium (0 V) for the three junctions (Figures 6 and S23−S26). We note that an electron transfer takes place between the BTTF unit and the top electrode (Figure S34), which induces an interface dipole

https://dx.doi.org/10.1021/acsami.0c15435
ACS Appl. Mater. Interfaces XXXX, XXX, XXX−XXX

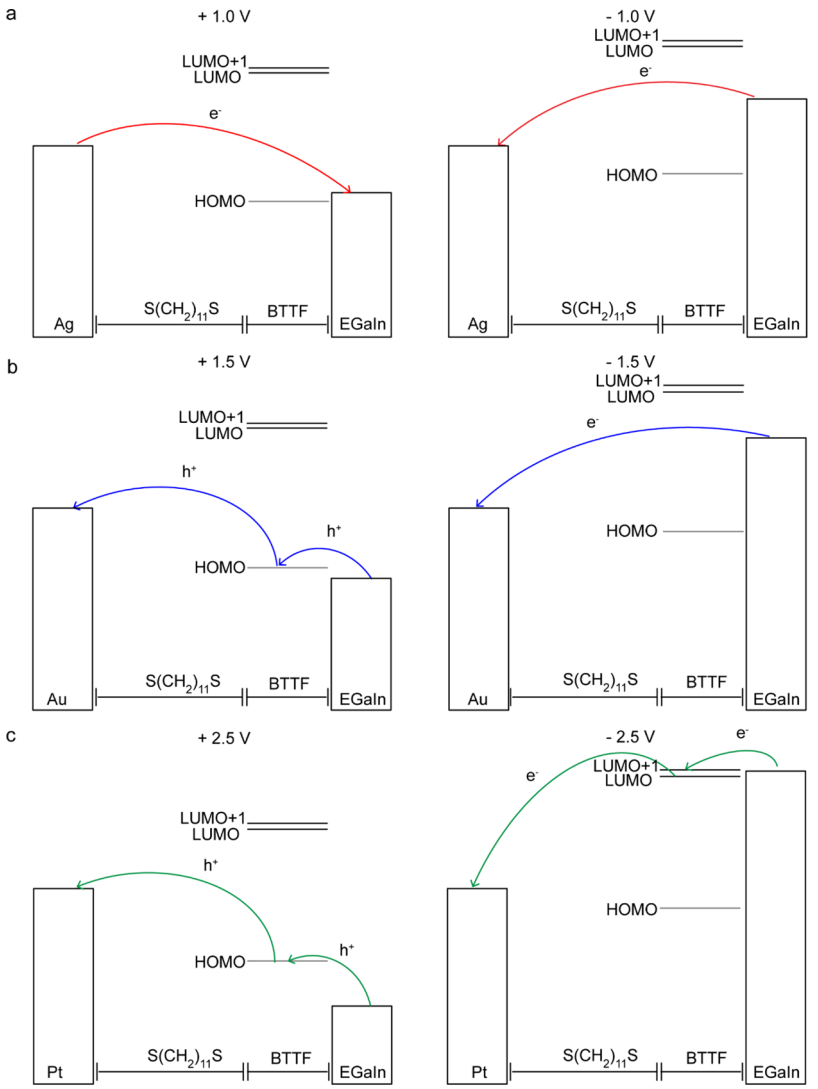

Figure 7. Energy level diagrams of M−S$(CH_2)_{11}$S−BTTF//GaO_x/EGaIn junctions with M = Ag (a), Au (b), and Pt (c). Φ_{SAM} and Φ_{EGaIn} are the work functions of the bottom electrode and top electrode after SAM formation. The arrows indicate the charge-transport process. The energy level diagrams were constructed based on the experimentally obtained E_{HOMO}, E_{LUMO}, and Φ_{SAM} values from UPS and NEXAFS. A renormalization factor of 1.5 (see ref 63) was used to correct for the change of the energy offset when adding a second electrode.

that downshifts the energetic levels of the SAMs. Consequently, the HOMO level in the junctions is not anymore in resonance with E_f as it was the case in the SAMs, but δE_H increases to ∼0.9 eV as determined from the transmission spectra in Figure 6. Similar shifts are also observed for the LUMO levels.

The transmission spectra across the junctions as a function of voltage were calculated by coupling the nonequilibrium Green's function theory (NEGF) to the DFT formalism using the Quantum ATK 2017.2 package (Figure 6). Because of the Fermi level pinning effects with the bottom electrode described in detail in the previous section, the transmission at negative/positive bias polarities is governed by unoccupied/occupied levels as indicated by the purple and orange lines in Figure 6. From the transmission spectra, the origin of the reversal of rectification, despite similarities in energy level alignment, becomes clear, as shown in Figure 7. In the case of Ag junctions, no energy levels fall in the relatively narrow bias window of ±1.0 V (Figure 6a). For junctions with Au, δE_H is smaller than δE_L (Figure 6b), in agreement with the XPS and NEXAFS results (Table 1), indicating that the HOMO dominates the mechanism of charge transport at a positive bias resulting in rectification (Figure 7b). The participation of the HOMO in the charge-transport mechanism was further confirmed by temperature-dependent $J(V)$ measurements on Au junctions reported in ref 62, which demonstrated that at a positive bias, the charge transport is thermally activated. In contrast, for junctions with Pt, at a large applied bias, the LUMO dominates the mechanism of charge transport at a negative bias. Although the HOMO is still involved with charge transport at a positive bias, its contribution to the charge transport is very weak in comparison with the LUMO level because another unoccupied orbital (LUMO + 1) is very close in energy to the LUMO (Figure 6c) and contributes significantly to charge transport at a large negative bias (Figure 7c), so that both levels are participating in the transport for −2.5 V. Thus, the calculations are in full agreement with the experimental data and explain in detail why the direction of rectification changes as a function of M. We would like to highlight that the calculations also show that the mechanism of charge transport would be similar for the three types of

https://dx.doi.org/10.1021/acsami.0c15435
ACS Appl. Mater. Interfaces XXXX, XXX, XXX−XXX

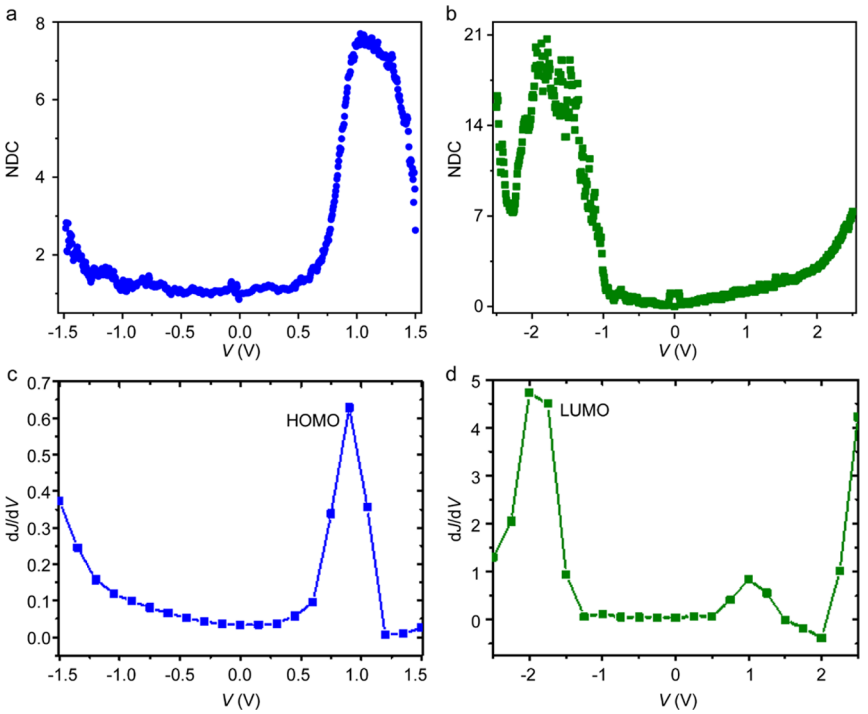

Figure 8. NDC plots for M−S$(CH_2)_{11}$S−BTTF//GaO_x/EGaIn junction where M = Au (a) and Pt (b). Calculated dJ/dV vs applied voltage curves for Au (c) and Pt (d) junctions.

junctions in the hypothetical case that Ag- and Au-based junction could withstand the same large applied bias as Pt.

According to the UPS measurements, $\delta E_H \approx 0.60$ eV (Table 1), but the calculations suggest that this level should enter the bias window around 1 V bias. Similarly, the NEXAFS results indicate that $\delta E_H \approx 1.8$ eV, while the calculations indicate that the LUMO enters the bias window around 1.5 eV. However, in these measurements, the top electrode is not present, but the DFT calculations show that charge transfer between BTTF and the top electrode results in a downshift of the energy levels of 0.5 eV when moving from large to close top electrode contacts (see Figure S31). We have estimated this downshift from the transition voltages both theoretically (Section S5) and experimentally (Section S6) as the maximum of the dJ/dV versus applied bias functions to identify the energetic positions of the conduction orbitals. We performed normalized differential conduction (NDC) analysis using eq 5 for the individual $J(V)$ traces.[64−66]

$$\mathrm{NDC} = \frac{\mathrm{d}J}{\mathrm{d}V}\cdot\frac{V}{J} = \frac{\mathrm{d}(\log J)}{\mathrm{d}(\log V)} \tag{5}$$

Figure 8a shows the NDC curve obtained from an Au−S$(CH_2)_{11}$S−BTTF//GaO_x/EGaIn junction with a resonance peak at +1.03 V. This peak indicates that the HOMO enters the conduction window at this bias.[67,68] At a negative bias, the NDC curve shows typical parabolic behavior with NDC increasing to NDC = 3, which is characteristic for off-resonant tunneling.[64] The NDC curve for a Pt−S$(CH_2)_{11}$S−BTTF//GaO_x/EGaIn junction (Figure 8b) is dominated by a resonance peak at −1.79 V, indicating that the LUMO dominates the mechanism of charge transport at this voltage. Figure 8c−d shows the theoretical dJ/dV versus V curves which mimic the experimental NDC plots very well. Figure 8c shows the HOMO resonance at +0.9 V for junctions with M = Au, which corresponds very well to the peak observed in the NDC plot shown in Figure 8a. Likewise, Figure 8d shows a peak at −2.0 V corresponding to a resonance of the LUMO, which matches very well the NDC plot shown in Figure 8b for the same junction. We note that the small HOMO peak in Figure 8d is visible at 1.0 V, but this peak is not resolved in the experimental data (Figure 8b). In the experimental data, the resonance for Pt is very broad. Likely at a positive bias, the HOMO is too broad to be seen as a clear peak, which could explain why the NDC curve for Pt at a positive bias does not follow clear parabolic behavior, but instead the NDC value gradually increases with V. In summary, the agreement between experiments and theory indicates that introduction of the top electrode results in a downshift in energies of the molecular levels of about 0.4 eV.

However, the calculated increase of the currents, once a molecular frontier orbital enters the conduction window, is much lower than the experimentally observed ones. Therefore, the experimental rectification ratios are between 1 and 2 orders of magnitude higher than the calculated ratios (Figure S36). It is important to note that our theoretical approach is used to model the charge transport only in the coherent regime and not in the incoherent hopping regime.[69,70] Preliminary data indicate that indeed hopping is important when a molecular frontier orbital falls in the conduction window (similar to molecular diodes based on ferrocene units),[29] but this change in the mechanism of charge transport from coherent to incoherent tunneling has not been accounted for in the current theory, and therefore the theory might underestimate the values of R for this reason. Moreover, our NEGF-DFT calculations primarily aim at providing reliable trends to rationalize experiments rather than a quantitative description of the energy level alignment in the junction due to the inherent limitations of DFT to predict accurate electronic gaps, especially in the proximity of metallic electrodes.

https://dx.doi.org/10.1021/acsami.0c15435
ACS Appl. Mater. Interfaces XXXX, XXX, XXX−XXX

CONCLUSIONS

Usually, it is challenging to tune the energy level alignment of molecular junctions because of Fermi level pinning. Consequently, it is still not straightforward to control the electronic functions of junctions, such as the direction of rectification. Most approaches to control rectification focus on chemical alteration of the molecular component of the junctions, but systematic studies involving different electrode materials are rare. Changes in the work function of the electrode have an effect on the magnitude and/or direction of interface dipoles, but often this effect is masked when the functional group couples too strongly with the electrode.[29,30] In this work, the BTTF redox unit is decoupled from the bottom electrode by the alkyl chain, making it possible to investigate interfacial charge transfer across the metal-thiolate bond and from the metal to the BTTF unit in detail. With the aid of detailed DFT calculations, the contributions of charge transfer across the metal−molecule interface involving the thiol-anchoring group and the redox-active unit in the SAMs as a function of three different metals with large differences in work functions (M = Ag, Au, and Pt) were elucidated. By using different metals, the bias window could be increased from ±1.0 V for Ag to ±2.5 V for Pt, making it possible to change the mechanism of rectification from HOMO-dominated charge transport at a low applied bias for junctions with Au to LUMO-dominated charge transport for junctions with Pt at a large bias. The change in the energy level alignment of the system upon application of a certain bias resulted in reversal of rectification in molecular diodes with EGaIn top electrodes. In other words, we have demonstrated a new way of tuning the direction of rectification by changing the bottom electrode material of the junction rather than by chemical alteration of the molecular structure which involves (often time-consuming) chemical synthesis. Our work provides new insights into the understanding of energy level alignment in molecular junctions with redox groups, which provide energetically accessible energy levels and are important toward the rational design of molecular junctions in general.

EXPERIMENTAL SECTION

Synthesis and characterization of the SAM precursor $(S(CH_2)_{11}S-BTTF)_2$ (Section S1), preparation of the bottom electrodes and SAMs (Section S2), surface characterizations of the SAMs (Section S3) (including time-of-flight secondary ion mass spectrometry, water contact angle measurements, AR XPS, UPS, NEXAFS, cyclic voltammetry, UV−vis measurements), junction formation and statistical analysis (Section S4), DFT calculations of BTTF SAMs and BTTF SAM-based junctions (Section S5), and normalized differential conductance analysis (Section S6) are provided in the Supporting Information.

ASSOCIATED CONTENT

Supporting Information

The Supporting Information is available free of charge at https://pubs.acs.org/doi/10.1021/acsami.0c15435.

Synthesis of $(S(CH_2)_{11}S-BTTF)_2$, preparation of SAMs, characterization of SAMs, junction fabrication and statistical analysis, and DFT calculations (PDF)

AUTHOR INFORMATION

Corresponding Authors

Jérôme Cornil − *Laboratory for Chemistry of Novel Materials, University of Mons, Mons 7000, Belgium;* orcid.org/0000-0002-5479-4227; Email: jerome.cornil@umons.ac.be

Jaume Veciana − *Institut de Ciéncia de Materials de Barcelona (ICMAB-CSIC)/CIBER-BBN, Bellaterra 08193, Spain;* orcid.org/0000-0003-1023-9923; Email: vecianaj@icmab.es

Christian A. Nijhuis − *Department of Chemistry and Centre for Advanced 2D Materials and Graphene Research Center, National University of Singapore, Singapore 117543 Singapore;* orcid.org/0000-0003-3435-4600; Email: chmnca@nus.edu.sg

Authors

Yingmei Han − *Department of Chemistry, National University of Singapore, Singapore 117543 Singapore*

Maria Serena Maglione − *Institut de Ciéncia de Materials de Barcelona (ICMAB-CSIC)/CIBER-BBN, Bellaterra 08193, Spain*

Valentin Diez Cabanes − *Laboratory for Chemistry of Novel Materials, University of Mons, Mons 7000, Belgium*

Javier Casado-Montenegro − *Institut de Ciéncia de Materials de Barcelona (ICMAB-CSIC)/CIBER-BBN, Bellaterra 08193, Spain*

Xiaojiang Yu − *Singapore Synchrotron Light Source, National University of Singapore, Singapore 117603 Singapore*

Senthil Kumar Karuppannan − *Department of Chemistry, National University of Singapore, Singapore 117543 Singapore*

Ziyu Zhang − *Department of Chemistry, National University of Singapore, Singapore 117543 Singapore*

Núria Crivillers − *Institut de Ciéncia de Materials de Barcelona (ICMAB-CSIC)/CIBER-BBN, Bellaterra 08193, Spain;* orcid.org/0000-0001-6538-2482

Marta Mas-Torrent − *Institut de Ciéncia de Materials de Barcelona (ICMAB-CSIC)/CIBER-BBN, Bellaterra 08193, Spain;* orcid.org/0000-0002-1586-005X

Concepció Rovira − *Institut de Ciéncia de Materials de Barcelona (ICMAB-CSIC)/CIBER-BBN, Bellaterra 08193, Spain;* orcid.org/0000-0002-2365-9479

Complete contact information is available at: https://pubs.acs.org/10.1021/acsami.0c15435

Author Contributions

#Y.H., M.S.M., and V.D.C. contributed equally.

Notes

The authors declare no competing financial interest.

ACKNOWLEDGMENTS

The authors express thanks to the Ministry of Education (MOE) for supporting this research under award nos. MOE2018-T2-1-088 and R-143-000-B30-112. We also acknowledge the Prime Minister's Office, Singapore, under its Medium Sized Centre program for supporting this research. This work was also funded by ITN iSwitch 642196, the DGI (Spain), projects FANCY (CTQ2016-80030-RA), GENESIS (PID2019-111682RB-I00) and MOTHER (MAT2016-80826-R), the Generalitat de Catalunya (2017-SGR-918), the Instituto de Salud Carlos III, through "Acciones CIBER", and the Spanish Ministry of Economy and Competitiveness through the "Severo Ochoa" program for Centers of Excellence in R&D (FUNFUTURE; CEX2019-000917-S). The work in Mons was financially supported by the EC through the Marie

Curie project ITN iSwitch (GA no. 642196). Computational resources were provided by the Consortium des Équipements de Calcul Intensif (CÉCI) funded by the Belgian National Fund for Scientific Research (F.R.S.-FNRS) under grant 2.5020.11. J.C. is an FNRS research director.

REFERENCES

(1) Kaneko, M.; Okada, T. Charge Transport in Molecular Catalysis in a Heterogeneous Phase. In *Molecular Catalysts for Energy Conversion*; Springer: Berlin, Heidelberg, 2009; pp 37−65.
(2) Amdursky, N.; Marchak, D.; Sepunaru, L.; Pecht, I.; Sheves, M.; Cahen, D. Electronic Transport Via Proteins. *Adv. Mater.* **2014**, *26*, 7142−7161.
(3) Wang, Q.; Ma, D. Management of Charges and Excitons for High-Performance White Organic Light-Emitting Diodes. *Chem. Soc. Rev.* **2010**, *39*, 2387−2398.
(4) Du, W.; Han, Y.; Hu, H.; Chu, H.-S.; Annadata, H. V.; Wang, T.; Tomczak, N.; Nijhuis, C. A. Directional Excitation of Surface Plasmon Polaritons Via Molecular through-Bond Tunneling across Double-Barrier Tunnel Junctions. *Nano Lett.* **2019**, *19*, 4634−4640.
(5) de Nijs, B.; Benz, F.; Barrow, S. J.; Sigle, D. O.; Chikkaraddy, R.; Palma, A.; Carnegie, C.; Kamp, M.; Sundararaman, R.; Narang, P.; Scherman, O. A.; Baumberg, J. J. Plasmonic Tunnel Junctions for Single-Molecule Redox Chemistry. *Nat. Commun.* **2017**, *8*, 994.
(6) Han, Y.; Nickle, C.; Zhang, Z.; Astier, H. P. A. G.; Duffin, T. J.; Qi, D.; Wang, Z.; del Barco, E.; Thompson, D.; Nijhuis, C. A. Electric-Field-Driven Dual-Functional Molecular Switches in Tunnel Junctions. *Nat. Mater.* **2020**, *19*, 843−848.
(7) Kumar, S.; Merelli, M.; Danowski, W.; Rudolf, P.; Feringa, B. L.; Chiechi, R. C. Chemical Locking in Molecular Tunneling Junctions Enables Nonvolatile Memory with Large on−Off Ratios. *Adv. Mater.* **2019**, *31*, 1807831.
(8) Wani, I. H.; Jafri, S. H. M.; Warna, J.; Hayat, A.; Li, H.; Shukla, V. A.; Orthaber, A.; Grigoriev, A.; Ahuja, R.; Leifer, K. A Sub 20 nm Metal-Conjugated Molecule Junction Acting as a Nitrogen Dioxide Sensor. *Nanoscale* **2019**, *11*, 6571−6575.
(9) Yan, H.; Bergren, A. J.; McCreery, R.; Della Rocca, M. L.; Martin, P.; Lafarge, P.; Lacroix, J. C. Activationless Charge Transport across 4.5 to 22 nm in Molecular Electronic Junctions. *Proc. Natl. Acad. Sci. U.S.A.* **2013**, *110*, 5326−5330.
(10) Kumar, K. S.; Pasula, R. R.; Lim, S.; Nijhuis, C. A. Long-Range Tunneling Processes across Ferritin-Based Junctions. *Adv. Mater.* **2016**, *28*, 1824−1830.
(11) Yuan, L.; Wang, L.; Garrigues, A. R.; Jiang, L.; Annadata, H. V.; Anguera Antonana, M.; Barco, E.; Nijhuis, C. A. Transition from Direct to Inverted Charge Transport Marcus Regions in Molecular Junctions Via Molecular Orbital Gating. *Nat. Nanotechnol.* **2018**, *13*, 322−329.
(12) Migliore, A.; Schiff, P.; Nitzan, A. On the Relationship between Molecular State and Single Electron Pictures in Simple Electrochemical Junctions. *Phys. Chem. Chem. Phys.* **2012**, *14*, 13746−13753.
(13) Thomas, J. O.; Limburg, B.; Sowa, J. K.; Willick, K.; Baugh, J.; Briggs, G. A. D.; Gauger, E. M.; Anderson, H. L.; Mol, J. A. Understanding Resonant Charge Transport through Weakly Coupled Single-Molecule Junctions. *Nat. Commun.* **2019**, *10*, 4628.
(14) Galperin, M.; Ratner, M. A.; Nitzan, A.; Troisi, A. Nuclear Coupling and Polarization in Molecular Transport Junctions: Beyond Tunneling to Function. *Science* **2008**, *319*, 1056.
(15) Heimel, G.; Romaner, L.; Zojer, E.; Bredas, J.-L. The Interface Energetics of Self-Assembled Monolayers on Metals. *Acc. Chem. Res.* **2008**, *41*, 721−729.
(16) Braun, S.; Salaneck, W. R.; Fahlman, M. Energy-Level Alignment at Organic/Metal and Organic/Organic Interfaces. *Adv. Mater.* **2009**, *21*, 1450−1472.
(17) Cahen, D.; Kahn, A.; Umbach, E. Energetics of molecular interfaces. *Mater. Today* **2005**, *8*, 32−41.
(18) Amsalem, P.; Niederhausen, J.; Wilke, A.; Heimel, G.; Schlesinger, R.; Winkler, S.; Vollmer, A.; Rabe, J. P.; Koch, N. Role of Charge Transfer, Dipole-Dipole Interactions, and Electrostatics in Fermi-Level Pinning at a Molecular Heterojunction on a Metal Surface. *Phys. Rev. B: Condens. Matter Mater. Phys.* **2013**, *87*, 035440.
(19) Hofmann, O. T.; Egger, D. A.; Zojer, E. Work-Function Modification Beyond Pinning: When Do Molecular Dipoles Count? *Nano Lett.* **2010**, *10*, 4369−4374.
(20) Egger, D. A.; Zojer, E. Anticorrelation between the Evolution of Molecular Dipole Moments and Induced Work Function Modifications. *J. Phys. Chem. Lett.* **2013**, *4*, 3521−3526.
(21) Obersteiner, V.; Egger, D. A.; Heimel, G.; Zojer, E. Impact of Collective Electrostatic Effects on Charge Transport through Molecular Monolayers. *J. Phys. Chem. C* **2014**, *118*, 22395−22401.
(22) Chen, X.; Annadata, H. V.; Kretz, B.; Zharnikov, M.; Chi, X.; Yu, X.; Egger, D. A.; Nijhuis, C. A. Interplay of Collective Electrostatic Effects and Level Alignment Dictates the Tunneling Rates across Halogenated Aromatic Monolayer Junctions. *J. Phys. Chem. Lett.* **2019**, *10*, 4142−4147.
(23) Aviram, A.; Ratner, M. A. Molecular Rectifiers. *Chem. Phys. Lett.* **1974**, *29*, 277−283.
(24) Bayat, A.; Lacroix, J.-C.; McCreery, R. L. Control of Electronic Symmetry and Rectification through Energy Level Variations in Bilayer Molecular Junctions. *J. Am. Chem. Soc.* **2016**, *138*, 12287−12296.
(25) Baghbanzadeh, M.; Belding, L.; Yuan, L.; Park, J.; Al-Sayah, M. H.; Bowers, C. M.; Whitesides, G. M. Dipole-Induced Rectification Across Ag^{TS}/SAM//Ga_2O_3/EGaIn Junctions. *J. Am. Chem. Soc.* **2019**, *141*, 8969−8980.
(26) Kovalchuk, A.; Egger, D. A.; Abu-Husein, T.; Zojer, E.; Terfort, A.; Chiechi, R. C. Dipole-Induced Asymmetric Conduction in Tunneling Junctions Comprising Self-Assembled Monolayers. *RSC Adv.* **2016**, *6*, 69479−69483.
(27) Ai, Y.; Kovalchuk, A.; Qiu, X.; Zhang, Y.; Kumar, S.; Wang, X.; Kühnel, M.; Nørgaard, K.; Chiechi, R. C. In-Place Modulation of Rectification in Tunneling Junctions Comprising Self-Assembled Monolayers. *Nano Lett.* **2018**, *18*, 7552−7559.
(28) Atesci, H.; Kaliginedi, V.; Celis Gil, J. A.; Ozawa, H.; Thijssen, J. M.; Broekmann, P.; Haga, M.-a.; van der Molen, S. J. Humidity-Controlled Rectification Switching in Ruthenium-Complex Molecular Junctions. *Nat. Nanotechnol.* **2018**, *13*, 117−121.
(29) Chen, X.; Roemer, M.; Yuan, L.; Du, W.; Thompson, D.; del Barco, E.; Nijhuis, C. A. Molecular Diodes with Rectification Ratios Exceeding 10^5 Driven by Electrostatic Interactions. *Nat. Nanotechnol.* **2017**, *12*, 797−803.
(30) Yuan, L.; Nerngchamnong, N.; Cao, L.; Hamoudi, H.; del Barco, E.; Roemer, M.; Sriramula, R. K.; Thompson, D.; Nijhuis, C. A. Controlling the Direction of Rectification in a Molecular Diode. *Nat. Commun.* **2015**, *6*, 6324.
(31) Zhang, G.-P.; Wang, S.; Wei, M.-Z.; Hu, G.-C.; Wang, C.-K. Tuning the Direction of Rectification by Adjusting the Location of the Bipyridyl Group in Alkanethiolate Molecular Diodes. *J. Phys. Chem. C* **2017**, *121*, 7643−7648.
(32) Nguyen, Q. V.; Martin, P.; Frath, D.; Della Rocca, M. L.; Lafolet, F.; Barraud, C.; Lafarge, P.; Mukundan, V.; James, D.; McCreery, R. L.; Lacroix, J.-C. Control of Rectification in Molecular Junctions: Contact Effects and Molecular Signature. *J. Am. Chem. Soc.* **2017**, *139*, 11913−11922.
(33) Otero, R.; Vázquez de Parga, A. L.; Gallego, J. M. Electronic, Structural and Chemical Effects of Charge-Transfer at Organic/Inorganic Interfaces. *Surf. Sci. Rep.* **2017**, *72*, 105−145.
(34) Vilan, A. (Invited) Energy Alignment at the Molecule - Electrode Interface: An Electrochemical-Potential/Hardness View. *ECS Trans.* **2018**, *86*, 67−78.
(35) Haag, R.; Rampi, M. A.; Holmlin, R. E.; Whitesides, G. M. Electrical Breakdown of Aliphatic and Aromatic Self-Assembled Monolayers Used as Nanometer-Thick Organic Dielectrics. *J. Am. Chem. Soc.* **1999**, *121*, 7895−7906.
(36) Yuan, L.; Jiang, L.; Nijhuis, C. A. The Drive Force of Electrical Breakdown of Large-Area Molecular Tunnel Junctions. *Adv. Funct. Mater.* **2018**, *28*, 1801710.

https://dx.doi.org/10.1021/acsami.0c15435
ACS Appl. Mater. Interfaces XXXX, XXX, XXX−XXX

(37) Joachim, C.; Ratner, M. A. Molecular Electronics: Some Views on Transport Junctions and Beyond. *Proc. Natl. Acad. Sci. U.S.A.* **2005**, *102*, 8801−8808.
(38) Paulson, B. P.; Miller, J. R.; Gan, W.-X.; Closs, G. Superexchange and Sequential Mechanisms in Charge Transfer with a Mediating State between the Donor and Acceptor. *J. Am. Chem. Soc.* **2005**, *127*, 4860−4868.
(39) Yuan, L.; Jiang, L.; Thompson, D.; Nijhuis, C. A. On the Remarkable Role of Surface Topography of the Bottom Electrodes in Blocking Leakage Currents in Molecular Diodes. *J. Am. Chem. Soc.* **2014**, *136*, 6554−6557.
(40) Jiang, L.; Sangeeth, C. S. S.; Wan, A.; Vilan, A.; Nijhuis, C. A. Defect Scaling with Contact Area in Egain-Based Junctions: Impact on Quality, Joule Heating, and Apparent Injection Current. *J. Phys. Chem. C* **2015**, *119*, 960−969.
(41) Souto, M.; Díez-Cabanes, V.; Yuan, L.; Kyvik, A. R.; Ratera, I.; Nijhuis, C. A.; Cornil, J.; Veciana, J. Influence of the Donor Unit on the Rectification Ratio in Tunnel Junctions Based on Donor−Acceptor Sams Using Ptm Units as Acceptors. *Phys. Chem. Chem. Phys.* **2018**, *20*, 25638−25647.
(42) Jiang, L.; Yuan, L.; Cao, L.; Nijhuis, C. A. Controlling Leakage Currents: The Role of the Binding Group and Purity of the Precursors for Self-Assembled Monolayers in the Performance of Molecular Diodes. *J. Am. Chem. Soc.* **2014**, *136*, 1982−1991.
(43) Yuan, L.; Thompson, D.; Cao, L.; Nerngchangnong, N.; Nijhuis, C. A. One Carbon Matters: The Origin and Reversal of Odd-Even Effects in Molecular Diodes with Self-Assembled Monolayers of Ferrocenyl-Alkanethiolates. *J. Phys. Chem. C* **2015**, *119*, 17910−17919.
(44) Gnatek, D.; Schuster, S.; Ossowski, J.; Khan, M.; Rysz, J.; Krakert, S.; Terfort, A.; Zharnikov, M.; Cyganik, P. Odd−Even Effects in the Structure and Stability of Azobenzene-Substituted Alkanethiolates on Au(111) and Ag(111) Substrates. *J. Phys. Chem. C* **2015**, *119*, 25929−25944.
(45) Chen, J.; Chang, B.; Oyola-Reynoso, S.; Wang, Z.; Thuo, M. Quantifying Gauche Defects and Phase Evolution in Self-Assembled Monolayers through Sessile Drops. *ACS Omega* **2017**, *2*, 2072−2084.
(46) Simão, C.; Mas-Torrent, M.; Casado-Montenegro, J.; Otón, F.; Veciana, J.; Rovira, C. A Three-State Surface-Confined Molecular Switch with Multiple Channel Outputs. *J. Am. Chem. Soc.* **2011**, *133*, 13256−13259.
(47) Marchante, E.; Maglione, M. S.; Crivillers, N.; Rovira, C.; Mas-Torrent, M. A Four-State Capacitance Molecular Switch Based on a Redox Active Tetrathiafulvalene Self-Assembled Monolayer. *RSC Adv.* **2017**, *7*, 5636−5641.
(48) Bard, A. J.; Faulkner, L. R. *Electrochemical Methods: Fundamentals and Applications*; John Wiley & Sons: New York, 2001.
(49) Yokota, Y.; Miyazaki, A.; Fukui, K.-i.; Enoki, T.; Tamada, K.; Hara, M. Dynamic and Collective Electrochemical Responses of Tetrathiafulvalene Derivative Self-Assembled Monolayers. *J. Phys. Chem. B* **2006**, *110*, 20401−20408.
(50) Kattel, B.; Wang, T.; Kafle, T. R.; Chan, W.-L. The Thickness of the Two-Dimensional Charge Transfer State at the TTF-TCNQ Interface. *Org. Electron.* **2017**, *48*, 371−376.
(51) Wang, Z.; Dong, H.; Li, T.; Hviid, R.; Zou, Y.; Wei, Z.; Fu, X.; Wang, E.; Zhen, Y.; Nørgaard, K.; Laursen, B. W.; Hu, W. Role of Redox Centre in Charge Transport Investigated by Novel Self-Assembled Conjugated Polymer Molecular Junctions. *Nat. Commun.* **2015**, *6*, 7478.
(52) Reus, W. F.; Nijhuis, C. A.; Barber, J. R.; Thuo, M. M.; Tricard, S.; Whitesides, G. M. Statistical Tools for Analyzing Measurements of Charge Transport. *J. Phys. Chem. C* **2012**, *116*, 6714−6733.
(53) Love, J. C.; Estroff, L. A.; Kriebel, J. K.; Nuzzo, R. G.; Whitesides, G. M. Self-Assembled Monolayers of Thiolates on Metals as a Form of Nanotechnology. *Chem. Rev.* **2005**, *105*, 1103−1170.
(54) Xie, Z.; Bâldea, I.; Smith, C. E.; Wu, Y.; Frisbie, C. D. Experimental and Theoretical Analysis of Nanotransport in Oligophenylene Dithiol Junctions as a Function of Molecular Length and Contact Work Function. *ACS Nano* **2015**, *9*, 8022−8036.
(55) Heimel, G.; Romaner, L.; Zojer, E.; Brédas, J.-L. Toward Control of the Metal−Organic Interfacial Electronic Structure in Molecular Electronics: A First-Principles Study on Self-Assembled Monolayers of π-Conjugated Molecules on Noble Metals. *Nano Lett.* **2007**, *7*, 932−940.
(56) Smith, C. E.; Xie, Z.; Bâldea, I.; Frisbie, C. D. Work Function and Temperature Dependence of Electron Tunneling through an N-Type Perylene Diimide Molecular Junction with Isocyanide Surface Linkers. *Nanoscale* **2018**, *10*, 964−975.
(57) Fonseca Guerra, C. l.; Handgraaf, J.-W.; Baerends, E. J.; Bickelhaupt, F. M. Voronoi Deformation Density (Vdd) Charges: Assessment of the Mulliken, Bader, Hirshfeld, Weinhold, and Vdd Methods for Charge Analysis. *J. Comput. Chem.* **2004**, *25*, 189−210.
(58) Diez-Cabanes, V.; Gonzalez, S. R.; Osella, S.; Cornil, D.; Van Dyck, C.; Cornil, J. Energy Level Alignment at Interfaces between Au (111) and Thiolated Oligophenylenes of Increasing Chain Size: Theoretical Evidence of Pinning Effects. *Adv. Theory Simul.* **2018**, *1*, 1700020.
(59) Rodriguez-Gonzalez, S.; Xie, Z.; Galangau, O.; Selvanathan, P.; Norel, L.; Van Dyck, C.; Costuas, K.; Frisbie, C. D.; Rigaut, S.; Cornil, J. Homo Level Pinning in Molecular Junctions: Joint Theoretical and Experimental Evidence. *J. Phys. Chem. Lett.* **2018**, *9*, 2394−2403.
(60) Kim, B.; Choi, S. H.; Zhu, X.-Y.; Frisbie, C. D. Molecular Tunnel Junctions Based on Π-Conjugated Oligoacene Thiols and Dithiols between Ag, Au, and Pt Contacts: Effect of Surface Linking Group and Metal Work Function. *J. Am. Chem. Soc.* **2011**, *133*, 19864−19877.
(61) Chiechi, R. C.; Weiss, E. A.; Dickey, M. D.; Whitesides, G. M. Eutectic Gallium-Indium (EGaIn): A Moldable Liquid Metal for Electrical Characterization of Self-Assembled Monolayers. *Angew. Chem.* **2008**, *47*, 142−144.
(62) Han, Y. M.; Nickle, C.; Maglione, M. S.; Karuppannan, S. K.; Casado-Montenegro, J.; Qi, D. C.; Chen, X. P.; Tadich, A.; Cowie, B.; Mas-Torrent, M.; Rovira, C.; Cornil, J.; Veciana, J.; Barco, E. D.; Nijhuis, C. A. Bias-Polarity Dependent Direct and Inverted Marcus Charge Transport Affecting Rectification in a Redox-Active Molecular Junction. Manuscript submitted.
(63) Yuan, L.; Breuer, R.; Jiang, L.; Schmittel, M.; Nijhuis, C. A. A Molecular Diode with a Statistically Robust Rectification Ratio of Three Orders of Magnitude. *Nano Lett.* **2015**, *15*, 5506−5512.
(64) Vilan, A. Revealing Tunnelling Details by Normalized Differential Conductance Analysis of Transport across Molecular Junctions. *Phys. Chem. Chem. Phys.* **2017**, *19*, 27166−27172.
(65) Vilan, A. Analyzing Molecular Current-Voltage Characteristics with the Simmons Tunneling Model: Scaling and Linearization. *J. Phys. Chem. C* **2007**, *111*, 4431−4444.
(66) Karuppannan, S. K.; Hongting, H.; Troadec, C.; Vilan, A.; Nijhuis, C. A. Ultrasmooth and Photoresist-Free Micropore-Based EGaIn Molecular Junctions: Fabrication and How Roughness Determines Voltage Response. *Adv. Funct. Mater.* **2019**, *29*, 1904452.
(67) Fereiro, J. A.; Yu, X.; Pecht, I.; Sheves, M.; Cuevas, J. C.; Cahen, D. Tunneling Explains Efficient Electron Transport Via Protein Junctions. *Proc. Natl. Acad. Sci. U.S.A.* **2018**, *115*, No. E4577.
(68) Hayakawa, R.; Hiroshiba, N.; Chikyow, T.; Wakayama, Y. Single-Electron Tunneling through Molecular Quantum Dots in a Metal-Insulator-Semiconductor Structure. *Adv. Funct. Mater.* **2011**, *21*, 2933−2937.
(69) Brédas, J.-L.; Beljonne, D.; Coropceanu, V.; Cornil, J. Charge-Transfer and Energy-Transfer Processes in π-Conjugated Oligomers and Polymers: A Molecular Picture. *Chem. Rev.* **2004**, *104*, 4971−5004.
(70) Coropceanu, V.; Cornil, J.; da Silva Filho, D. A.; Olivier, Y.; Silbey, R.; Brédas, J.-L. Charge Transport in Organic Semiconductors. *Chem. Rev.* **2007**, *107*, 926−952.

https://dx.doi.org/10.1021/acsami.0c15435
ACS Appl. Mater. Interfaces XXXX, XXX, XXX−XXX